

A drop on a floating sheet: boundary conditions, topography and formation of wrinkles†

Cite this: *Soft Matter*, 2013, **9**, 8289

K. Bugra Toga,^a Jiangshui Huang,^{ab} Kevin Cunningham,^c Thomas P. Russell^{*a} and Narayanan Menon^{*b}

The radial wrinkle pattern generated by a liquid drop on a floating elastic sheet has stimulated a number of advances in the understanding of wrinkle patterns in ultrathin sheets. A puzzle associated with the spatial extent of this simple, highly symmetric pattern has only recently been resolved, but several other basic aspects of the pattern remain unexplained. Our previous experiments have studied the extent and wavenumber of the pattern via 2-dimensional images. In the current study we report a full 3-dimensional topographical characterization of this archetypical problem, and of its counterpart, a bubble beneath a sheet. In addition to measurements of the wrinkle amplitude, these studies reveal the elastic deformation and the resulting wrinkle pattern beneath the drop. We also show that the flat boundary condition at the contact line of the drop is achieved by a cascade of wrinkles on both sides of the boundary. Finally, we report studies by high-speed video imaging of the propagation of the wrinkle pattern, with the unexpected result that the wavenumber is established early in the development of the pattern, before it has reached its full spatial extent.

Received 14th March 2013

Accepted 29th May 2013

DOI: 10.1039/c3sm50736j

www.rsc.org/softmatter

Introduction

The buckling instability of thin elastic sheets supported on deformable substrates¹ has been exploited in a wide variety of applications such as the measurement of material properties^{2–5} and cellular motility,^{6–9} the fabrication of tunable optic gratings¹⁰ and colloidal crystal assemblies,^{1,11} control of adhesion,¹² roughness^{13,14} and surface topography.¹⁵ A full understanding of the wrinkling of supported sheets is of enormous practical value. In this article we report a detailed experimental characterization of the wrinkle pattern generated on an elastic sheet floating on a fluid, due to the capillary stresses of a drop placed on the sheet. Our previous study of this simple, symmetric, well-characterized setting showed that the traditional post-buckling approach is inadequate to characterize the wrinkle patterns. This stimulated a number of conceptual advances in the understanding of elastic instabilities on ultrathin sheets. Our new experimental observations pose some fresh puzzles and can also benchmark new theoretical development.

Due to the growing practical importance of soft elastic substrates in stretchable electronics, in microfluidics, and in

biological applications, the vast majority of experiments on thin-film buckling have studied sheets supported on elastic foundations. However, both for conceptual clarity and for experimental precision and ease, a thin film floating on a liquid surface^{2,16–18} offers considerable benefits. First, the ability to relax on the fluid allows for homogeneous initial conditions, whereas any nonuniform pinning to a soft substrate leads to quenched in-plane stresses in the film. Second, the static response of the fluid is trivially simple and local, whereas forces in an elastic substrate are long-range, and lead to nontrivial effects from boundaries and finite thickness of the substrate. Third, a solid substrate applies both normal and shear forces at the interface with the film whereas a fluid does not apply shear. Fourth, it is difficult to apply uniform external forces and boundary conditions by direct mechanical clamping and manipulation, whereas the capillary forces applied by a liquid are homogeneous, small enough so as not to cause plastic deformation, and can be continuously dialed in with surfactants or mixtures. Finally, a soft substrate can have slow intrinsic viscoelastic or poroelastic relaxation times, leading to nontrivial kinetic effects, whereas a fluid has a simple viscous response.

Placing a droplet of water on an elastic film floating on water generates a wrinkle pattern of finite extent as shown in the image in Fig. 1A. The film is stretched radially at its outer edge by the air–water surface tension. As the sketch in Fig. 1A shows, the droplet applies a Laplace pressure normal to the sheet, and a line tension at the contact line of the drop. If the resultant in-plane radial tension at the contact line is sufficiently larger than the outside tension, then the film is pulled radially toward the

^aDepartment of Polymer Science and Engineering, University of Massachusetts, Amherst, MA 01003, USA. E-mail: russell@mail.pse.umass.edu

^bDepartment of Physics, University of Massachusetts, Amherst, MA 01003, USA. E-mail: menon@physics.umass.edu

^cDepartment of Chemical Engineering, University of Massachusetts, Amherst, MA 01003, USA

† Electronic supplementary information (ESI) available. See DOI: 10.1039/c3sm50736j

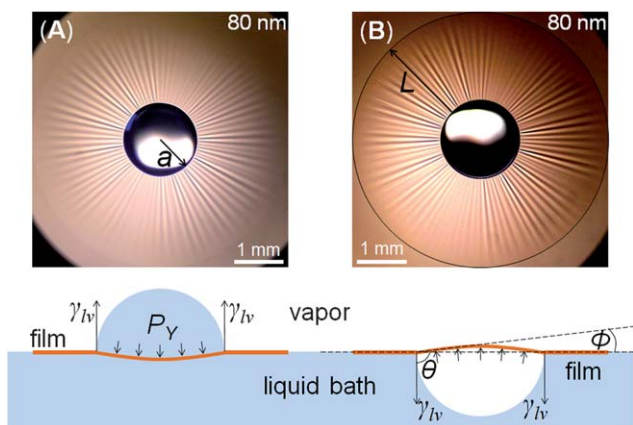


Fig. 1 Optical micrographs of (A) a droplet (of radius $a = 0.74$ mm) and (B) a bubble ($a = 0.79$ mm) wrinkling a floating sheet of polystyrene (thickness $t = 80$ nm). The schematic diagrams show the capillary forces at the contact line, and the Laplace pressure P_Y acting on the sheet. We also label the contact angle θ , and the angle ϕ above or below the horizontal due to the deformation of the sheet under the drop or bubble. The diameter of the sheet is 23 mm, much greater than the field of view.

contact line and the resultant build-up of material can induce buckling in the azimuthal direction.

This radially symmetric wrinkle pattern can be characterized by the length, L , and number, N , of the wrinkles formed. Huang *et al.*² studied the dependence of N and L as a function of the film thickness, t , and the droplet size, a . The number of wrinkles, was successfully described by scaling arguments adapted from ref. 19 as $N \sim (\gamma a^2/B)^{1/4}$, where the bending modulus, $B = Et^3/12(1 - \lambda^2)$, is determined by the thickness t , the Young's modulus E , and the Poisson ratio λ , and γ is the air–water surface tension. To understand the length of wrinkles, Huang *et al.* employed an analysis for an annulus placed under differential tension.²⁰ This calculation, attributed to Lamé,²¹ proceeds by computing the radial and azimuthal stresses σ_{rr} and $\sigma_{\theta\theta}$ in the unbuckled state of the film with the boundary conditions specified by the radial tensions T_i and T_o ($<T_i$) being applied at the inner radius ($r = a$) and the distant outer edge of the film, respectively. When $T_i/T_o > 2$, the azimuthal stress becomes compressive within some radius, which is then identified as the extent of the wrinkled zone. The extent of the wrinkles, L , is then $L \sim af(T_i/T_o)$ when the ratio of the tensions exceeds the threshold value. However, the experiments indicate that the wrinkle length is dependent not only on the radius a , but also the thickness of the sheet, consistent with a scaling of the form $L \sim at^{1/2}$. To recover dimensional consistency, the scaling $L \sim a(Et/\gamma)^{1/2}$ was used and achieved a satisfactory empirical description of the data.

Taken together, these equations for N and L lead to a simple metrology that yields the Young's modulus, E , and the thickness t in terms of the measured quantities. To provide a more solid footing for the scaling for L , Vella *et al.*²² performed a full post-buckling calculation for the Lamé geometry, including a microscopic calculation for the radial stress at the contact line based on a balance of the stresses in the sheet with the liquid–vapour surface tension at the contact line.²³ This calculation did produce a thickness-dependence to L , but which has a different functional

form than experimentally observed, and under-predicts the observed length of wrinkles. The failure of this textbook analysis for the size L of the buckled region in this simple, highly symmetric geometry indicated a fundamental weakness in our understanding of the buckling of ultrathin films. A fundamentally different issue was raised by Davidovitch *et al.*²⁴ in their study of an annular region under differential tension. They suggest that for thin enough sheets, the traditional post-buckling, near-threshold (NT) approach is questionable. They introduce a new dimensionless number called the “bendability”, which, in contrast to the purely geometric aspect ratio t/X (where X is the relevant in-plane dimension) also incorporates the mechanical properties of the sheet. When the bendability $1/\epsilon = X^2\gamma/B$ is large enough, they point out that the stress state of a sheet even slightly beyond the buckling threshold is profoundly affected by the presence of wrinkles and is not properly described by considering perturbations to the unbuckled state. Rather, they propose that the correct treatment of the wrinkled state involves a perturbation about the so-called membrane limit of a sheet with zero bending-resistance. This calculation framework builds upon the intuitive basis of tension-field theory.²⁵ Bending rigidity is introduced as a correction to this basic far-from-threshold (FT) picture. The FT framework has also been tested experimentally in a different geometry.²⁶

Recently, a full FT analysis of the drop-on-sheet geometry in combination with a correct treatment of the radial stress balance at the contact line has shown good agreement with the measured length, L , as a function of the experimental control parameters.²⁷

However, there is much richness that remains to be explored and understood in this very simple experimental setting. As an obvious matter, the next-order calculation for a small but finite bending modulus that yields the number of wrinkles, N , has yet to be done. There is also currently no calculation for the wrinkle profile in this geometry, though a numerical solution³⁴ has been computed for the annulus geometry which predicts a sharply defined wrinkle tip in the zero-thickness limit, with an additional boundary layer for finite thickness.

In order to fully experimentally characterize the wrinkled phase, we present in this article 3-dimensional characterizations of the elastic deformation both outside the contact line and under the drop, both of which were missing in the original experiments of Huang *et al.* In particular, we present a detailed characterization of the boundary conditions for the wrinkle at the contact line. We find that the flat boundary condition at the contact line of the drop is achieved by a cascade of wrinkle refinement on both sides of the boundary. Finally, the inception and evolution of the wrinkle pattern are studied in the early times following the application of the capillary stresses to the sheet.

Experimental setting

As shown in Fig. 1A a wrinkle pattern is generated by first floating a thin polystyrene (PS) sheet on the surface of a fluid, and then placing a drop in the centre of the film with a blunt-tip micropipette. For the data we show in this article, the diameter of the sheet is always bigger than the size L of the wrinkle pattern, so that the wrinkle pattern is unaffected by edge effects.

The drop size is increased in small increments by adding more fluid. The drop radii range from $a = 0.2$ to 1 mm. In this range of drop radii, no plastic deformation of the sheet is observed.

In Fig. 1B we demonstrate an alternative way of creating a wrinkle pattern governed by a balance of the same physical forces. Here, we release an air bubble within the fluid bath under the sheet. The bubble attaches to the sheet and shortly thereafter attains the equilibrium shape shown in the sketch in Fig. 1B. We are able to observe the effect of varying bubble radius due to diffusion of the gas through the PS sheet, forced by Laplace pressure. This process is very slow, so that mechanical equilibrium may be assumed at all times. The bubble-under-sheet protocol may be a useful tool in situations where it is not easy to deliver a drop to the top surface, for instance, if the sheet is sandwiched at the interface between two fluids or if the upper fluid is inaccessible. For the purposes of this article, the advantage of the bubble-under-sheet geometry is that it exposes the region in the interior of the contact line to direct visual inspection and bright-field microscopy.

Materials

Large-aspect-ratio sheets were prepared from dilute solutions of linear PS (Polymer Source, Atactic, M_n 91k, M_w 95k) in toluene spin coated onto clean microscope slides. In experiments with a gas bubble, we sometimes used higher molecular weight linear PS (Polymer Source, Atactic, M_n 520k, M_w 876k) to suppress gas permeability. The thickness of the PS sheets ($t = 30$ to 300 nm) was separately measured by an X-ray diffractometer or white-light interferometry. Circles of diameter 23 mm were scribed on the PS film. These were floated onto the surface of a pool of deionized water² by inserting the scribed edges of the film into the water.

The aspect ratio or von Kármán number of the sheet is extremely high, ranging from $a/t = 10^3$ to 10^5 . The bendability of the sheet under the applied tension, $1/\varepsilon = a^2\gamma/B$ is also extremely large, with ε ranging from 2×10^2 to 3×10^6 .

For the experiments reported here, the fluid in the drop is deionized water. The fluid in the bath is either glycerol or water. The effect of continuously varying surface tension by mixtures or by adding surfactant has been reported elsewhere.²⁷

Observations and results

Wrinkle length and wavenumber in two geometries

We begin by discussing the equivalence between the drop-on-sheet and bubble-under-sheet geometries more quantitatively. As can be seen in Fig. 1, in both geometries, the radial tension applied to the free edge of the sheet is γ_{lv} . The sheet also experiences an out-of-plane force at the contact line, again due to the surface tension γ_{lv} . Both bubble and drop apply a uniform Laplace pressure on the sheet. In the case where the fluid is water and sheet is PS, we measure a contact angle of 88 – 90° , with no observable contact angle hysteresis so that the drop or bubble is a hemisphere. In either case, the Laplace pressure is $P_Y = 2\gamma_{lv}/a$. However, in our experiments, the drop is small enough that the weight of the drop is much smaller than the

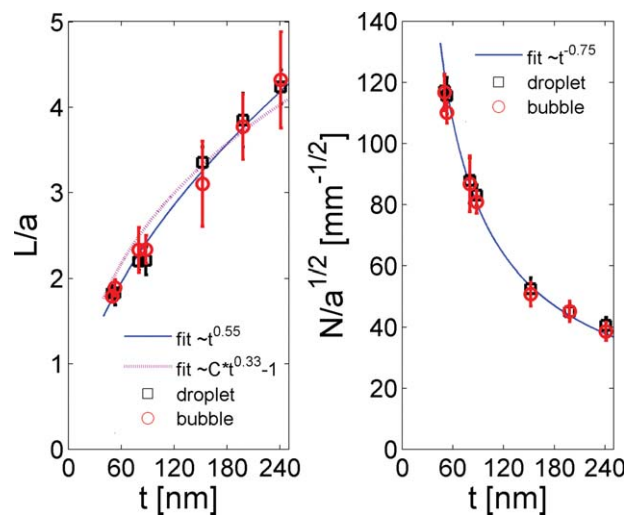


Fig. 2 (A) The length L and (B) the number N of wrinkles are scaled by the radius a of the contact line, and plotted against film thickness t . Error bars correspond to the standard deviation of data collected for several values of a . In (A), the blue solid line ($L/a = 0.205t^{0.55}$) is a best fit to a power law (as in ref. 2), while the dotted line shows the functional form $L/a + 1 = Ct^{1/3}$ (as in ref. 27). The number of wrinkles, N , scales with the square root of a and as $B^{-1/4}$ ($N/a^{0.50} = 2310t^{-0.75}$).

capillary force, $P_Y a^2 \gg \rho g a^3$. We can thus expect identical external stresses on the sheet.

In Fig. 2 we show data for the length, L , and number, N , of the wrinkles obtained in these two geometries. At each value of film thickness, t , data are taken at several values of drop and bubble radius a . As in ref. 2 we find that $L \propto a$, so we plot the scaled length of the wrinkles, L/a , against the thickness, t , of the sheet. As shown in Fig. 2A the data are experimentally indistinguishable in these two geometries. The data for both are consistent with our previous finding² of $L/a = C_l(Y/\gamma)^{1/2}$ where the stretching modulus $Y = Et$. The square-root dependence on thickness is indicated by the fit-line. For a given thickness, we find the number of wrinkles, $N \propto (a)^{1/2}$ and therefore in Fig. 2B we show $N/(a)^{1/2}$ versus thickness t . This choice of ordinate allows us to collapse several values of a in a single data point. The number of wrinkles, N , is also found to be similar in the two geometries. The solid line is fit to a $t^{-3/4}$ dependence on thickness, once again consistent with our previous finding that $N = C_2(\gamma a^2/B)^{1/4} \propto a^{1/2}t^{-3/4}$.

We recall that in our original work,² we followed a scaling argument that produced a correct description of these data for the wrinkle number, while the wrinkle length was a puzzle. The situation has now been reversed, in that a new FT calculation has been shown to be consistent with these data for the size of the wrinkle pattern,²⁷ whereas theory has yet to converge with experiment on the wavenumber of the wrinkle pattern. In what follows, we outline observations that we trust will stimulate a resolution of this new puzzle.

Contact angle and geometry inside the contact line

At its free edge, the sheet is tugged at with a radial line tension γ_{lv} . However, the radial tension σ_{rr} at the contact line is a more complex issue. As sketched in Fig. 3B, the sheet deforms into a

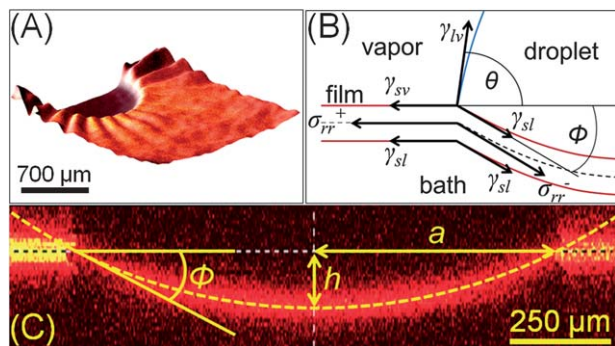


Fig. 3 Confocal microscopy was used to characterize the topography of sheets deformed by droplets. (A) A perspective image is shown for a film ($t = 209$ nm) wrinkled by a droplet with $a = 0.5$ mm. The scale bar shows the in-plane scale; the out-of-plane axis is exaggerated. (B) Force balance at the contact line. (C) A vertical plane through a diameter demonstrates the bulge in film ($t = 33$ nm) under a droplet with $a = 0.56$ mm. The vertical axis is exaggerated and not to scale. The horizontal dashed line represents the bath level. The vertical dashed line goes through the center, where the bulge height $h = 36.6$ μm .

spherical cap under the drop or bubble. The sheet is then subject to out-of-plane forces near the contact line whose magnitudes are known, but whose directions are affected by the elastic deformation of the sheet. In this section, we determine experimentally the 3D geometry of the sheet near the contact line in order to fully specify the external forces acting on the sheet.

We emphasize that the geometry of the drop near the contact line cannot be inferred from the usual Young–Laplace formula for force balance between the horizontal components of γ_{lv} , γ_{sv} , and γ_{ls} , since this approach is predicated on the idea that any resultant vertical force component is balanced by the underlying solid substrate. However, the sheet deforms in response to the vertical component of the force, altering the geometry. This deviation from the Young–Laplace contact angle θ_Y also occurs in a different regime where the substrate is low-modulus and can stretch in response to capillary forces.^{28–30} A correct description of the contact angle requires a self-consistent calculation of the radial stress inside and outside the contact line, as well as the capillary forces.

To measure the shape of the sheet under the drop, we labelled the sheet with fluorescent dye and imaged it with confocal microscopy. In Fig. 3A, we show the reconstructed image of the deformed sheet. The bulge under the drop is evident. In Fig. 3C, we show a single vertical slice through a diameter of the drop. The height of the bulge, h , and the angle ϕ below the horizontal at the contact were measured for a number of sheets of different thickness, and for drops of different radii. Similar measurements of the 3D topography of the bubble geometry were also made. Since the bulge was at the upper exposed surface in this case, we were able to study the geometry by white-light interferometry, which is a faster and more precise technique.

In Fig. 4A we show data for the height of the bulge, h , as a function of drop radius, a , for four different thicknesses. The dependence on a is linear, leading us to show in Fig. 4B, h/a against thickness. We show in Fig. 4B the angle below the horizontal, ϕ , as a function of thickness. The angle ϕ was not observed to depend upon the drop radius. These two dimensionless

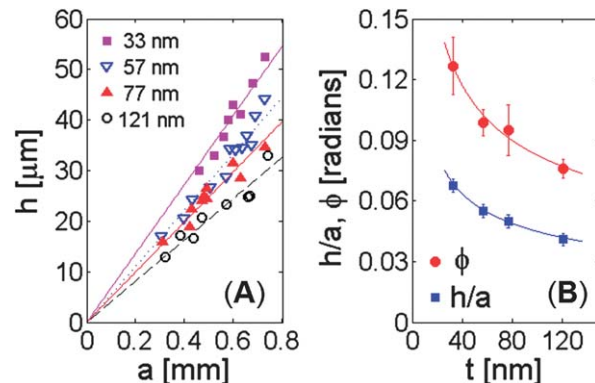


Fig. 4 (A) The height h of the bulge under the droplet scales linearly with the radius of the contact line, a . The bulge height is large in thinner films. (B) Bulge height h and the angle ϕ at the contact line decrease with film thickness. The solid lines show best-fit power laws with an exponent -0.38 .

descriptors of the bulge-shape both scale with thickness as $t^{-1/3}$. While we were not able to independently measure the angle θ shown in Fig. 3B, our data for the angle ϕ agrees with calculations, as shown in ref. 27. They further find that the deviation of the actual contact angle $\theta + \phi$ from the Young–Laplace angle is given by 2ϕ . With this understanding, it is also possible to compute θ from these data, thus leading to a full determination of all the forces labelled in Fig. 3B. The theoretical analysis of the radial force balance that determines the connection between geometry and stress is detailed in ref. 27.

Wrinkle pattern at contact line

In the previous section, we have ignored the additional complexity at the contact line due to the presence of the wrinkles. As is clear from all the images shown in this article, the wrinkles extend all the way to the contact line. Had the contact line been a free boundary, as in the annular Lamé geometry, then the wrinkle amplitude would have been greatest at the inner boundary. In the geometry we consider here, the contact line is not a free boundary and it is natural to ask whether and how the wrinkles terminate at the contact line.

In Fig. 5A, we show a bright-field micrograph of the pattern near the contact line of a bubble. This image reveals two remarkable features:

- There are wrinkles inside the contact line as well.
- The wrinkles both inside and outside the contact line undergo a cascade to higher wavenumber close to the contact line.

The first of these features may be seen to occur in a drop as well, as shown in the confocal fluorescence micrograph in Fig. 5B, and the second of these features is shown in a bright-field close-up of the wrinkle near the drop (Fig. 5C).

The existence of wrinkles within the drop is not surprising: as studied in ref. 26, a flat sheet constrained to live on a curved drop will experience compression at its edges, leading to wrinkles invading the sheet from the free edge. An experimental study of this geometry provided the first detailed validation of an FFT analysis for the scaling laws for the length of the wrinkles as a function of the stretching modulus, size of sheet,

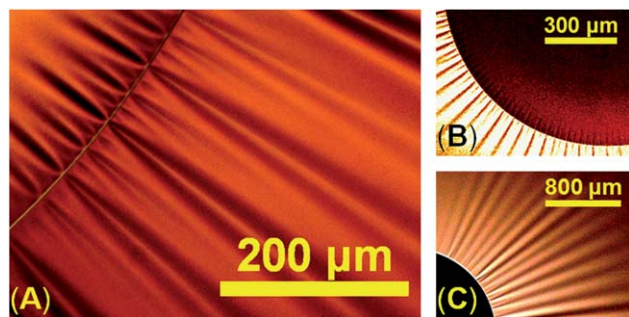


Fig. 5 Wavelength refinement near the contact line. (A) An optical micrograph of the sheet near a contact line of a bubble ($a = 0.95$ mm) under a PS film ($M_w = 876$ k; $t = 80$ nm). (B) A confocal image of the contact line drop ($a = 0.70$ mm) under a PS film ($M_w = 91$ k; $t = 33$ nm). (C) A bright-field image of the contact line drop ($a = 0.82$ mm) under a PS film ($M_w = 91$ k; $t = 93$ nm).

applied tension and imposed curvature.²⁶ However, the major difference between those wrinkles and the wrinkles in Fig. 5 is that the tips of both the inside and outside wrinkles terminate at the same contact line, which is not a free boundary.

This requirement on both inside and outside wrinkle patterns leads to the cascade that is shown in Fig. 5. To minimize wrinkle amplitude at the contact line, the wavenumber has to increase in order to preserve length in the azimuthal direction. A similar cascade phenomenon can be observed either when the edge is clamped flat (as happens at the top of a curtain),³¹ or when there is an energetic cost at the edge of a pattern.¹⁸ When there is tension in the wrinkle direction, such a wrinkle cascade typically proceeds smoothly, by the addition of new Fourier modes.^{32,33} As is also evident (most clearly in Fig. 5A), the inside and outside wrinkle patterns are in registry with each other.

In Fig. 6 we show the refinement of the pattern by plotting the number of wrinkles as a function of distance from the contact line, for two thicknesses and for two drop radii. The wrinkle cascade has a different characteristic length inside and outside the contact line. Inside the bubble, the wrinkle pattern does not develop a bulk value, with the wavenumber cascading down rapidly to zero. The wrinkle pattern extends considerably further outside the contact line; over a lengthscale that we label Δ , the wrinkle number $N(r)$ reaches the steady value N of the wavenumber. This lengthscale is scale shorter than the wrinkle length L .

The data in Fig. 6 suggest that the bubble radius has a stronger influence on the size Δ of the cascading region than does the thickness. In order to better quantify the dependence on these variables, we measure Δ for varying bubble radii, and for sheets of varying thickness. We obtain Δ from an analysis of the intensity $I(\theta, r)$ of the bright-field image of the wrinkle pattern. After filtering the image to remove low-frequency variations in intensity, we measure the standard deviation of intensity variation in the azimuthal direction, $\sigma_1(r)$, as a function of the radial distance from the contact line, r . $\sigma_1(r)$ has a peak at a value of r that marks the end of the wrinkle cascade; this measure is shown by the solid triangles in Fig. 6 to coincide with the location where $N(r)$ becomes independent of r .

The size of the cascade region was found to be proportional to the bubble radius. We therefore plot the scaled variable Δ/a

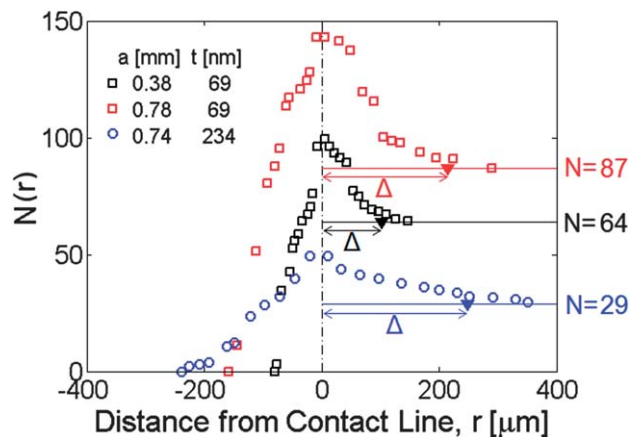


Fig. 6 The wrinkle wavenumber increases as the contact line is approached from either side. The data are taken in the bubble-under-sheet geometry with PS films ($M_w = 520$ k). The size of the cascading region outside the drop is labelled Δ .

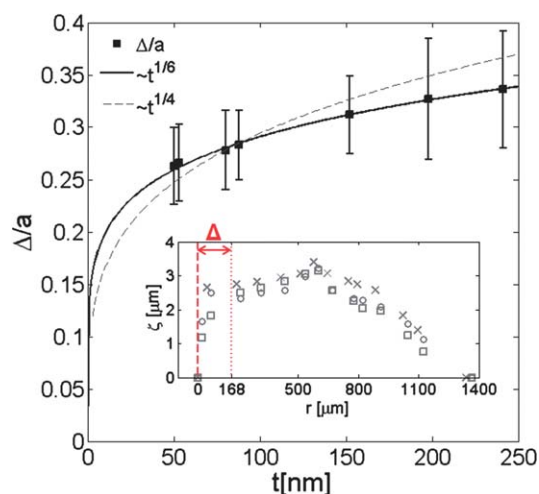


Fig. 7 The size of the cascading region Δ outside a droplet scales linearly with a . The dependence of Δ on t is weak with an empirical exponent, $1/6$. Inset: radial height profile of three neighboring wrinkles formed by a droplet ($a = 0.56$ mm) on PS sheet ($t = 77$ nm).

in Fig. 7, against t , the thickness of the sheet. The solid line shows a power-law fit $\sim t^{1/6}$. With this weak dependence, the data are perhaps even compatible with the penetration length of the cascade (Δ/a) being independent of thickness (as previously observed in a 1-dimensional, rectangular geometry¹⁸).

Wrinkle profile

Within the precision of the optical interferometry measurement, the contact line lies in a horizontal plane. A cut along an external wrinkle reveals a height profile $\zeta(r)$ that rises rapidly from the contact line in the cascade region *i.e.* for $r < \Delta$, as shown in the inset to Fig. 7. After a single-mode pattern emerges, the amplitude slowly dies away with increasing radius as shown in the image in Fig. 8A. The wrinkle has a definite terminus, showing that the length L is well-defined. The length L determined from bright-field images coincides with that determined from 3D imaging.

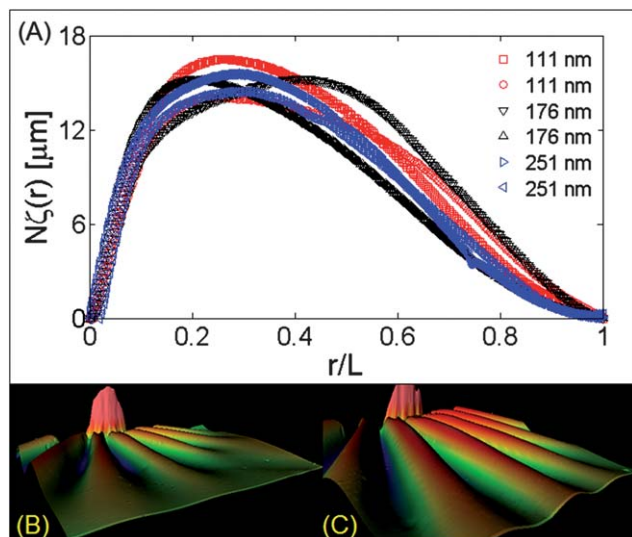


Fig. 8 (A) Profile of wrinkles along radial direction for PS (91k) sheets floating on a glycerol bath. The wrinkles are generated by bubbles and the data are obtained from 3D images acquired with an optical profilometer as shown below. (B) 176 nm thick PS (91k) film wrinkled by $a = 0.29$ mm bubble. (C) 176 nm thick PS (91k) film wrinkled by $a = 0.34$ mm bubble.

In Fig. 8A, we show the wrinkle profile $\zeta(r)$ multiplied by wrinkle number N for three sheet thicknesses, each at two drop radii. Within the variability of the experiment, we obtain a collapse of the wrinkle profile when plotted against the radial coordinate normalized by the wrinkle length r/L . A comparison of this shape would be a test of any theoretical development that goes beyond a correct scaling of the variables. The wrinkle profile has been computed in ref. 34 for the annulus geometry but not for a drop on a sheet.

Development of the wrinkle pattern

In the previous sections, we have discussed the attributes of the wrinkle pattern at mechanical equilibrium. Here we discuss the time-dependent development of the wrinkles immediately following the application of the capillary forces, as followed by high-speed video imaging.

For these measurements, we employ the bubble-under-sheet protocol. Following the release of the bubble in fluid, buoyancy drives it to the bottom surface of the sheet. After a latency period of a few milliseconds, the spherical bubble bursts and the contact line spreads, rapidly attaining its steady-state diameter.

The bursting of the bubble sets a sharp onset-time for the Laplace pressure and the line tension indicated in Fig. 3B. Thereafter, we see an elastic wave rippling outwards from the centre at a high speed, and the wrinkle pattern developing in its wake on a slower time-scale than the wavefront.

The time-dependence of the development of the length and number of the wrinkles is shown in Fig. 9. The steady-state diameter of the contact line is achieved with the first two milliseconds. As can be seen, the asymptotic values of N and L are established within tens of milliseconds. The surprising aspect of these data is that the final wavenumber is established much earlier in the development of the pattern than is the final

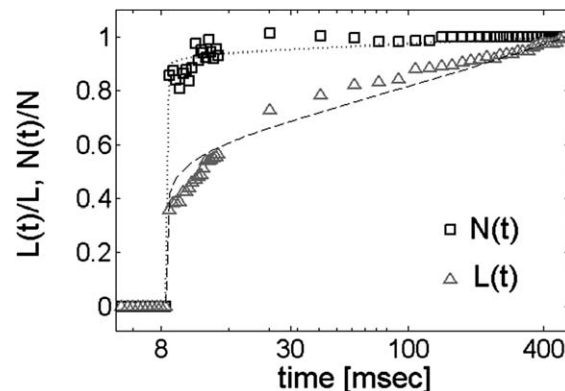


Fig. 9 Time dependence of the growth of the wrinkle pattern following the bursting of a bubble underneath a 62 nm PS sheet. N and L are obtained from bright-field images taken with a high-speed camera. An example of such a movie is given in the ESI.†

length of the wrinkles. This is rather surprising, since the basic idea of the FT theory that so successfully describes the spatial extent of the wrinkle pattern, is that the tension in the radial direction is the dominant energetic component in the pattern. To the first approximation (*i.e.* the leading order of approximation in an expansion in ε), the bending energy involved in forming the wrinkles is insignificant. Higher order terms in ε determine the wavenumber. It is therefore counterintuitive that the wavenumber, which is determined by a subtler contribution to the energy, establishes itself before the length of the wrinkle and the overall tensional stress state are fully determined.

Conclusions

The experimental protocol of placing a drop on a floating sheet, or its new counterpart, the bubble under the sheet, have already led to important new developments in our understanding of the wrinkling instability in ultrathin sheets. The results we present here raise new questions. We still lack a description of the 3D wrinkle profile. We do not understand the effect of the wrinkle cascade on either side of contact line. The wrinkle pattern on the inside and the outside of the contact line appear to be in registry with each other. This indicates that azimuthal variations in stress are communicated across the contact line. At a more elementary level, FT theoretical predictions for the wave number are still lacking. In the FT scenario, many wavelengths are unstable to buckling. Which of these are selected will depend on these subtler issues of matching interior and exterior wrinkle patterns at the contact line. These questions will need to be addressed to achieve a quantitative understanding of the wrinkle pattern, which will enable the use of this experimental setting as a metrology for the mechanical properties of thin films, or as a probe of surface energies. However, some of our observations challenge even the qualitative understanding of the mechanics of the wrinkle pattern. Why is it that in the development of the wrinkle pattern, the wrinkle wavenumber is established well before the wrinkle length? We speculate that the underlying explanation for both these observations lies in the fact that the wrinkle tip is always close to the buckling

threshold. Thus, it may be that the near-threshold energetic considerations determine the selection of wave number in the incipient pattern. The length of wrinkles could be subsequently determined by the stress field over the entire sheet, which may be relatively indifferent to the bending energy.

Methods

Image analysis

The wrinkle length, L , is determined both manually by finding the tip of the wrinkle in an image, as well as by an algorithm in which we measure the standard deviation in intensity in concentric circles around the drop and find the radius at which this quantity drops to the level of the noise. The wrinkle number N is determined by a manual count as well as by taking the intensity in a thin annulus centred at $r \approx 0.5L$, and determining the dominant fourier component in this profile.

3D imaging

A Leica DCSP2 fluorescent laser scanning confocal microscope was used to obtain 3D images. For these studies, the PS films were fluorescently labeled with a water-insoluble dye, Nile Red. Commercially available acupuncture needles were anchored around the perimeter of the film to trap the film and minimize motional blurring during the scan. The field of view of the FCM objective was $1.5 \text{ mm} \times 1.5 \text{ mm}$, and the in-plane lateral resolution was $\sim 0.1 \text{ }\mu\text{m}$. Vertical scan steps were made with a resolution of $0.6 \text{ }\mu\text{m}$.

A Zygo Interferometric microscope was used to obtain optical profilometry images of the bubble surface. For the greater stability needed here, we used a bath of glycerol rather than water. The field of view was $1.0 \text{ mm} \times 1.5 \text{ mm}$ with a $\sim 0.1 \text{ }\mu\text{m}$ in-plane resolution, and a vertical resolution of $\sim 1 \text{ nm}$. The vertical scan was done over a range of $40 \text{ }\mu\text{m}$. Each vertical slice takes 2 seconds to acquire. The volume of the bubble was constant during the scan.

Acknowledgements

We gratefully acknowledge support from the NSF-MRSEC on Polymers at UMass Amherst DMR 08-20506 (KBT, imaging), NSF DMR 09-07245 (NM) and DMR 12-0778 (NM). The research was initiated (JH) and continued (KBT, partial support) under DE-FG02-96ER45612 (TPR). We are thankful for valuable conversations with B. Davidovitch, R. Schroll, M. Adda-Bedia, and E. Cerda, and to the A. J. Crosby lab for the use of the optical interferometer.

Notes and references

- 1 K. Efimenko, M. Rackaitis, E. Manias, A. Vaziri, L. Mahadevan and J. Genzer, *Nat. Mater.*, 2005, **4**(4), 293–297.
- 2 J. Huang, M. Juskiewicz, W. H. de Jeu, E. Cerda, T. Emrick, N. Menon and T. P. Russell, *Science*, 2007, **317**(5838), 650–653.
- 3 E. A. Wilder, S. Guo, S. Lin-Gibson, M. J. Fasolka and C. M. Stafford, *Macromolecules*, 2006, **39**(12), 4138–4143.
- 4 C. M. Stafford, C. Harrison, K. L. Beers, A. Karim, E. J. Amis, M. R. Vanlandingham, H. C. Kim, W. Volksen, R. D. Miller and E. E. Simonyi, *Nat. Mater.*, 2004, **3**(8), 545–550.
- 5 A. J. Nolte, R. E. Cohen and M. F. Rubner, *Macromolecules*, 2006, **39**(14), 4841–4847.
- 6 A. K. Harris, P. Wild and D. Stopak, *Science*, 1980, **208**(4440), 177–179.
- 7 K. Burton and D. L. Taylor, *Nature*, 1997, **385**(6615), 450–454.
- 8 P. Uttayarat, G. K. Toworfe, F. Dietrich, P. I. Lelkes and R. J. Composto, *J. Biomed. Mater. Res., Part A*, 2005, **75**(3), 668–680.
- 9 X. Y. Jiang, S. Takayama, X. P. Qian, E. Ostuni, H. K. Wu, N. Bowden, P. LeDuc, D. E. Ingber and G. M. Whitesides, *Langmuir*, 2002, **18**(8), 3273–3280.
- 10 C. Harrison, C. M. Stafford, W. H. Zhang and A. Karim, *Appl. Phys. Lett.*, 2004, **85**(18), 4016–4018.
- 11 C. Lu, H. Möhwald and A. Fery, *Soft Matter*, 2007, **3**(12), 1530–1536.
- 12 E. P. Chan, E. J. Smith, R. C. Hayward and A. J. Crosby, *Adv. Mater.*, 2008, **20**(4), 711–716.
- 13 H. Yin, R. Huang, K. D. Hobart, Z. Suo, T. S. Kuan, C. K. Inoki, S. R. Shieh, T. S. Duffy, F. J. Kub and J. C. Sturm, *J. Appl. Phys.*, 2002, **91**(12), 9716–9722.
- 14 F. Iacopi, S. H. Brongersma and K. Maex, *Appl. Phys. Lett.*, 2003, **82**(9), 1380–1382.
- 15 S. Cai, D. Breid, A. J. Crosby, Z. Suo and J. W. Hutchinson, *J. Mech. Phys. Solids*, 2011, **59**(5), 1094–1114.
- 16 L. Pocivavsek, R. Dellsy, A. Kern, S. Johnson, B. Lin, K. Y. C. Lee and E. Cerda, *Science*, 2008, **320**(5878), 912–916.
- 17 B. D. Leahy, L. Pocivavsek, M. Meron, K. L. Lam, D. Salas, P. J. Viccaro, K. Y. C. Lee and B. Lin, *Phys. Rev. Lett.*, 2010, **105**, 058301.
- 18 J. Huang, B. Davidovitch, C. D. Santangelo, T. P. Russell and N. Menon, *Phys. Rev. Lett.*, 2010, **105**, 038302.
- 19 E. Cerda and L. Mahadevan, *Phys. Rev. Lett.*, 2003, **90**, 74302.
- 20 E. Cerda, *J. Biomech.*, 2005, **38**, 1598–1603.
- 21 S. P. Timoshenko and J. N. Goodier, *Theory of Elasticity*, McGrawHill, 1970.
- 22 D. Vella, M. Adda-Bedia and E. Cerda, *Soft Matter*, 2010, **6**, 5778–5782.
- 23 J. Olives, *J. Phys.: Condens. Matter*, 1993, **5**, 2081.
- 24 B. Davidovitch, R. D. Schroll, D. Vella, M. Adda-Bedia and E. A. Cerda, *Proc. Natl. Acad. Sci. U. S. A.*, 2011, **108**(45), 18227–18232.
- 25 E. H. Mansfield, *The Bending and Stretching of Plates*, Cambridge University Press, Cambridge, 1989.
- 26 H. King, R. D. Schroll, B. Davidovitch and N. Menon, *Proc. Natl. Acad. Sci. U. S. A.*, 2012, **109**(25), 9716–9720.
- 27 R. D. Schroll, M. Adda-Bedia, E. Cerda, J. Huang, N. Menon, T. P. Russell, K. B. Toga, D. Vella and B. Davidovitch, *Phys. Rev. Lett.*, 2013, submitted.
- 28 M. E. R. Shanahan and P. G. de Gennes, *Comptes Rendus de l'Académie des Sciences Série II*, 1986, vol. 302, p. 517.
- 29 R. W. Style and E. R. Dufresne, *Soft Matter*, 2012, **8**, 7177–7184.

- 30 R. W. Style, R. Boltysanskiy, Y. Che, J. S. Wettlaufer, L. A. Wilen and E. R. Dufresne, *Phys. Rev. Lett.*, 2013, **110**, 066103.
- 31 H. Vandeparre, M. Piñeira, F. Brau, B. Roman, J. Bico, C. Gay, W. Bao, C. N. Lau, P. M. Reis and P. Damman, *Phys. Rev. Lett.*, 2011, **106**, 22430.
- 32 P. Bella and R. V. Kohn, arXiv:1202.3160, 2012.
- 33 B. Davidovitch, *Phys. Rev. E: Stat., Nonlinear, Soft Matter Phys.*, 2009, **80**, 025202.
- 34 B. Davidovitch, R. D. Schroll and E. A. Cerda, *Phys. Rev. E: Stat., Nonlinear, Soft Matter Phys.*, 2012, **85**, 066115.